Nanoscale characterization of crystalline and amorphous phases in silicon oxycarbide ceramics using 4D-STEM

The corrections made in this section will be reviewed and approved by a journal production editor.

Ni Yang[a], Colin Ophus[b], Benjamin H. Savitzky[b], Mary C. Scott[b,c], Karen Bustillo[b], Kathy Lu[a,*] klu@vt.edu

[a]Department of Materials Science and Engineering, Virginia Polytechnic Institute and State University, Blacksburg, VA 24061, USA

[b]National Center for Electron Microscopy, Molecular Foundry, Lawrence Berkeley National Laboratory, 1 Cyclotron Road, Berkeley, CA 94720, USA

[c]Department of Materials Science and Engineering, University of California, Berkeley 94720, USA

*Corresponding author.

Abstract

Polymer-derived ceramics have great potentials in various high-temperature fields. However, lack of atomic-scale characterization and understanding of the short- to medium-range order and disorder hinders the advancement of this promising material family. In this study, poly(vinylmethylsiloxane)-derived silicon oxycarbide (SiOC) is used as a model system to address this issue. Electron diffraction-based radial distribution function (RDF) analysis is used to characterize the short- to medium-range order in the SiOC system and provide local structural data with a resolution of a few nanometers. With systematic data calibration and structural analysis, integrated 2D images from the diffraction pattern at each probe position are recorded and analyzed by the Python-based py4DSTEM toolkit; phase distributions of heterogeneous amorphous plus crystalline SiOC are obtained. This approach provides atomic-level characterization and can advance our fundamental understanding of the SiOC formation and microstructure evolution.

Keywords:

4D-STEM, Radial distribution function, Amorphous structure, SiOC, Crystallinity mapping

~~1.~~1 Introduction

Nanostructure analysis of amorphous plus crystalline phases in the polymer-derived ceramics (PDCs) is challenging due to their small sizes and mixed atomic arrangements [1]. Among these, polymer-derived silicon oxycarbide ceramics (SiOC) are amorphous in X-ray characterization studies but display structural heterogeneity at the nanometer length scale [2,3]. The oxygen and carbon atoms bond randomly to silicon in a three-dimensional covalent structure - mixed SiOC units (SiC_xO_{4-x}, $1 \leq x \leq 4$) [4,5]. Additionally, the structural characteristics of these SiOC units change progressively with the pyrolysis temperature, pyrolysis atmosphere, and polymeric precursors [6]. After pyrolysis at 800–1100 °C, SiOC glasses consist of a homogeneous network of mixed SiOC tetrahedrals and free carbon species [7, 8]. The system can be described as a nanocomposite composed of a SiOC matrix (including SiO_4, SiO_3C, SiO_2C_2, $SiOC_3$, and SiC_4 tetrahedrals) in which free carbon (amorphous C and turbostratic C) is dispersed. The microstructure is featureless at length scales larger than a few nanometers. At 1100–1300 °C, amorphous SiO_2 nanodomains form [9, 10]. At higher temperatures (1300–1450 °C), the amorphous network undergoes further phase separation, which enhances the formation of SiO_2-rich phase and C-rich phase, the latter being comprised of β-SiC nanocrystals and turbostratic carbon [11,12]. The microstructures at such high temperatures are amorphous plus crystalline. Due to the intriguing atomic structures and the wide application potentials of SiOCs, understanding of their continuously evolving atomic structures is needed.

Very few experimental techniques can provide a valid method to characterize the amorphous and crystalline mixed structures in SiOC materials. Traditional X-ray diffraction experiments with large sample areas lack spatial resolution,

especially at the nanoscale [3,13,14]. Neutron diffraction cannot effectively penetrate the bulk of the samples and examine discrete phases [15,16]. High-resolution TEM shows significantly smaller β-SiC crystal (2–10 nm) precipitates in the SiOC at temperatures above 1250 °C [3,17,18]. However, very careful sample preparation and proper location selection are needed in order to avoid mixed phases in the selected area for diffraction study. Also, the diffraction data are confined to the specific selected sites. Nuclear magnetic resonance (NMR) has been used to understand the bonding environments and the phase fractions of different amorphous SiOC units [2,11,19,20]. Undesirably, the data are an average representation of the entire sampling region, not at specific locations.

In conventional scanning transmission electron microscopy (STEM) imaging, the nano/microstructure of a thin sample is characterized by using a monolithic detector to integrate a subset of the scattered or unscattered electron beam at each probe position. However, recent advances in detector technologies and computational methods have enabled the recording of 2D images using a converged electron probe over a 2D grid of probe positions. This new approach is termed 4D-STEM, which has been applied to virtual imaging, orientation mapping, strain mapping, and differential phase-contrast [21–25]. For example, structural mapping of organic amorphous material ((6,6)-phenyl C61-butyric acid methyl ester and poly(3-hexylthiophene-2,5-diyl)) [26] has been made possible due to the very small spatial extent of the electron probe. 4D-STEM pair distribution function analysis has provided phase distributions of organic composites [27].

In this work, we use 4D-STEM experiments performed on SiOC samples to characterize the well-recognized heterogeneous, nanostructured, and mixed amorphous and crystalline structures in combination with radial distribution function (RDF) mapping. We demonstrate that RDF analysis of 4D-STEM diffraction patterns in a nano volume is a critical starting point in the characterization of amorphous and crystalline mixed SiOC materials. These RDF maps can be analyzed in order to distinguish different glassy phases [28] as well as crystalline regions. We show that this method is extremely sensitive to nanoscale structural variations in SiOC materials.

~~2.~~2 Materials and characterization

This work used a commercially available poly(vinylmethylsiloxane) (PVMS, MW = 1000–1500 g/mol, Gelest Inc., Morrisville, PA) as the base precursor to synthesize the corresponding SiOC ceramics. Specifically, the polymeric solutions were poured into ~~a~~ clean zirconia crucibles and placed into a tube furnace (1730–20 Horizontal Tube Furnace, CM Furnaces Inc., Bloomfield, NJ). The samples were pyrolyzed in an Ar atmosphere (AR 300, AirGas, Radford, VA) with a flow rate of about 900 std. cm^3/min at 1400 °C, with a heating rate of 1 °C/min for 2 h, and then cooled to 25 °C with a rate of 1 °C/min.

A Gatan Orius CCD camera installed on a FEI TitanX operating at an accelerating voltage of 300 kV was used to record the 4D-STEM diffraction patterns [22] with an exposure time of 50 ms. In real space, the scan positions were in a 50~~x~~ × 50 pixel grid with a step size of ~2 nm, resulting in a field of view of 100 nm~~x~~ × 100 nm. A probe forming aperture below the second condenser lens had an aperture size of 40 μm resulting in a quasi-parallel beam with a semi-convergence angle of 0.8 millirads. Generally speaking, a smaller semi-convergence angle generates a higher depth-of-field [29]. However, if the semi-convergence angle is too small, the size of the electron probe in real space increases and spatial resolution is compromised [30]. Thus, a proper semi-convergence angle is critical for obtaining high-quality 4D-STEM data for quantitative analysis and varies from material to material. The thickness and flatness of the examination area and the nature of the material determine the selection of a proper semi-convergence angle. The TEM samples made from SiOC ceramics are often thicker than other material types due to their brittle nature. The illumination condition formed an electron probe with a full-width-half-max of 1.2 nm.

py4DSTEM [31], a python-based software package developed by Lawrence Berkeley National Laboratory for analysis of 4D-STEM datasets, was applied to our dataset in this project. Py4DSTEM is open-source and supports many different modes of 4D-STEM analysis.

~~3.~~3 Results and discussion

~~3.1.~~3.1 Data processing and calibration

Several processing steps need to be applied to a 4D-STEM dataset in order to obtain an accurate analysis of the local structural information. Fig. 1(a) illustrates the average of all diffraction patterns from a raw dataset (PVMS-derived SiOC) and visualizes the location of a bright-field detector (shown in red).

alt-text: Fig. 1

~~Fig. 1.~~Fig. 1

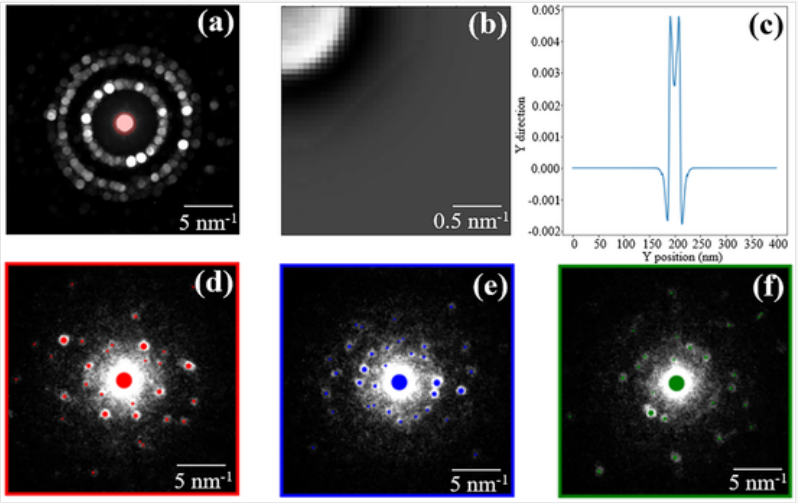

Bragg disk detection in the SiOC ceramic: (a) averaged diffraction pattern of 4D-STEM datacube (red shield – bright-field detector), (b) the vacuum probe template, (c) a kernel for cross correlation template matching with individual diffraction patterns, and (d-f) the detected Bragg disk positions. (For interpretation of the references to colour in this figure legend, the reader is referred to the web version of this article.)

To perform the Bragg disk detection and identify the reciprocal lattice points of the crystals in the SiOC ceramics [23, 29], the probe template in diffraction through vacuum was constructed and visualized in Fig. 1(b). It was generated from the average vacuum region in our 4D-STEM experimental scan, and its kernel (Fig. 1(c)) was formed by the Gaussian subtraction to normalize the probe template in order to improve the disk detection process. The position of Bragg disks was measured and is shown by colored masks in Fig. 1(d-f). The sizes of the colored circles indicate the relative disk intensity. The entire dataset was recorded with a frame size of 50 × 50 probe positions. The disk detection was performed for all of the 2500 diffraction patterns collected.

Shift correction is the most significant step to ensure the accuracy of the analysis results [31,32]. We have also corrected the diffraction shift due to probe de-scan (Fig. S1, Figs. 2(a)-(f)) as well as elliptical distortion correction and pixel size calibration (Figs. 2(g)-(h)).

alt-text: Fig. 2

~~Fig. 2.~~Fig. 2

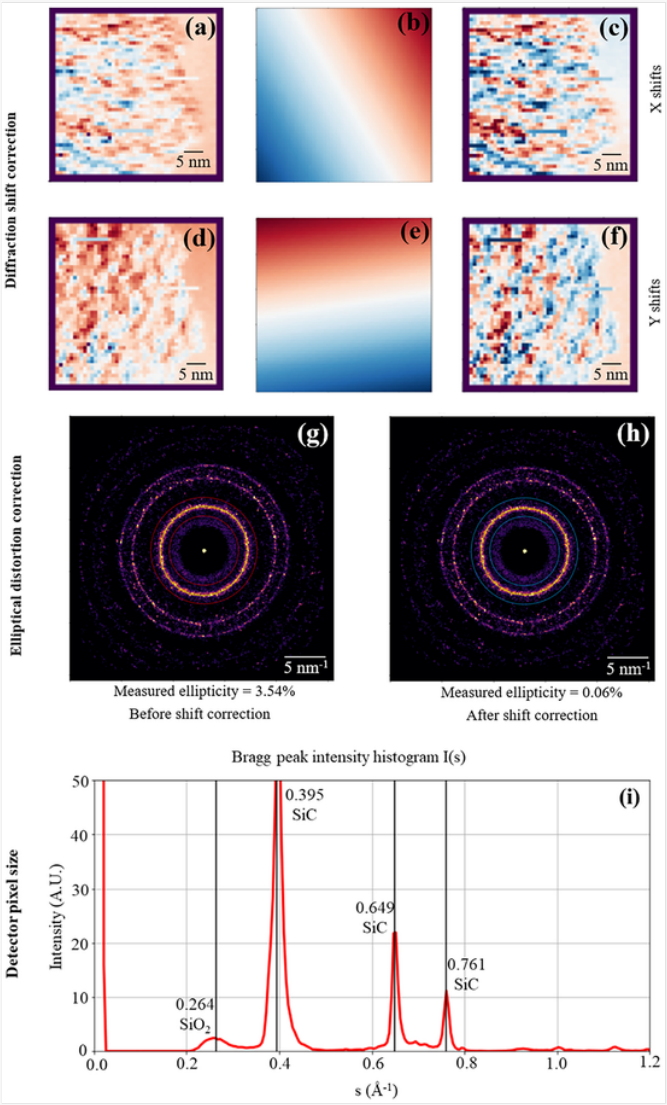

Calibration: (a-f) diffraction shift correction, (g-h) elliptical distortion correction, and (i) pixel size calibration.

In order to calibrate both the shifts of the pattern due to probe de-scan and the elliptical distortions introduced by misalignment from the optical axis or from the projector lenses of the STEM instrument, we used 2D histograms of the Bragg peak positions. We refer to these images as a “Bragg vector map,” which is shown in Fig. S1 of the supplement. After correcting for the probe descan, the Bragg vector map becomes sharper as shown in Fig. S1(a) and (b). It is noted that the sharpening differences between them are not evident because the beam shifts are very small due to the small region of the sample scanned [33]. Both before and after the diffraction shift correction, the diffraction patterns on the left side show the presence of amorphous halo rings along with crystal diffraction spots, which represent the mixed amorphous (SiC_xO_{4-x}, $1 \leq x \leq 4$) and crystalline (cristobalite and SiC) nature of SiOC, as discussed in the introduction section about phase evolution of SiOC with pyrolysis temperatures. The degree of the shift generally depends on the 4D-STEM parameters, such as camera length, real space scan, and instrument type [34].

The top row images in Fig. 2(a-f) show the correction of diffraction shifts generated from the position optic axis from one diffraction pattern to the next. It shows the measurement of the shift histograms and images for different diffraction patterns. Figs. 2(a) and (d) illustrate the initial measurements of shift at each position from the 4D-STEM images. After the diffraction shift correction for X (Fig. 2(h)) and Y (Fig. 2(e)) shifts, the corrected measurements in Figs. 2(e) and (f) show the shapes and pixels more clearly than before the correction (Figs. 2(a) and (d)). The circular features related to the optic axis are depicted in ellipses as illustrated in Figs. 2(g-h). These distortions must be corrected by fitting an elliptical function in the annular areas.

The bottom row of Fig. 2(i) reveals the calibration of the diffraction pixel size by measuring the cristobalite diffraction vectors with a known spacing. Fig. 2(i) shows the radial intensity of the elliptically corrected Bragg vector map in Fig. 2(h), and it matches well with the XRD reference data [14,35], showing the expected peaks at 0.264, 0.395, 0.649, and 0.761 1/Å. The peak at 0.394 1/Å (2.53 Å) corresponds well to the brightest SiC peak in the structure [36]. SiC also has rather strong peaks at 0.646 and 0.757 1/Å, in excellent agreement with the XRD pattern [6,13]. The brightest SiO_2 peak should be at 0.242 1/Å. However, the diffraction contribution from amorphous SiOC and even amorphous C shift the peak to 0.264 1/Å. It is the only large peak that does not originate from SiC. In fact, it is much broader and supports the hypothesis that it is from a different phase.

~~3.2.~~3.2 Radial distribution function

The most distinct features and signals from Fig. 2(h) are representative of the nanocrystalline components. The electron diffraction patterns of SiOC materials containing a substantial fraction of amorphous phases typically contain ring-like features with a radius given by a characteristic scattering length. Detailed structural information from the distance and density of neighboring shells of atoms can be obtained from a RDF analysis of the diffraction patterns. RDF [28] enables a concrete interpretation of the diffraction data in terms of interatomic distances and reveals reliable structural information of amorphous materials. The procedure for the combined 4D-STEM and RDF analysis includes data acquisition by recording the diffraction patterns in the STEM mode with a quasi-parallel nano-beam configuration (0.8 millirad semi-convergence angle and 1.2 nm probe size) over a 2D grid of probe positions. For the RDF analysis of the SiOC material, each experimental diffraction pattern is processed individually to determine a local RDF, from which detailed structural information is obtained. As explained in other studies [16,28], the diffraction profile I(s) needs to be normalized by subtracting the single atomic scattering factor $\varphi(s)$ as expressed in Eq. (1):

$$\varphi(s) = \frac{I(s) - N\langle f(s)^2\rangle}{N\langle f(s)\rangle^2} s \tag{1}$$

where N is the number of atoms within the volume sampled by the electron probe, s is the diffraction space, and $f(s)$ is the parameterized elemental scattering factor. The corresponding RDF $G(r)$ can be obtained by a sine Fourier transformation of the structure factor $\varphi(s)$ in all the diffraction space according to Eq. (2):

$$G(r) = \int_0^{S_{max}} \varphi(s) \sin(2\pi s r)\, ds \tag{2}$$

In reality, $\langle f(s) \rangle$ can only be treated as a rough approximation for the SiOC material because of mixed SiO_xC_y tetrahedrals. The diffraction profile $I(s)$ should be fitted by the average scattering factor $\varphi(s)$ across a range of angles and consistent with the real structure from the SiOC matrix.

To estimate the structure factors and the RDFs for the amorphous phases, the Bragg disks need to be masked off and median statistics should be used. Two radial integrals can be calculated based on the single image from Fig. 2(h) through a polar-elliptical transform as shown in Figs. 3(a) and (b) with a mask. It reveals the presence of a certain degree of Bragg scattering and therefore crystallinity, as well as the relationship between the diffraction intensity and optic axis distance. The resulting curve, I(q), is shown in Fig. 3(c). Clearly, there is a strong feature at 0.416 1/Å, and a weaker feature at 0.753 1/Å, which is due to the presence of the crystalline phases. However, these two obvious features vanish (curve in red) for the median statistics based on masked Bragg peaks. Usually, the presence of crystalli~~nities~~tes has minor effects on mean statistics, and it can be concluded that there is significant mixing between the ordered and disordered phases in this SiOC system. By fitting the thermal background at low q areas and atomic scattering factors at high q areas in Fig. 3(c), a structure factor, $\varphi(s)$, describing the arrangements of atoms in the SiOC materials, can be calculated in Fig. 3(d) for a given set of atomic species to high angle scattering. Compared to the static structure factor $\varphi(s)$ above, RDF is advantageous due to its clear physical meaning and simplicity. Thus, the RDF with a real space quantity (Fig. 4) is extracted from the structure factor $\varphi(s)$.

alt-text: Fig. 3

~~Fig. 3.~~Fig. 3

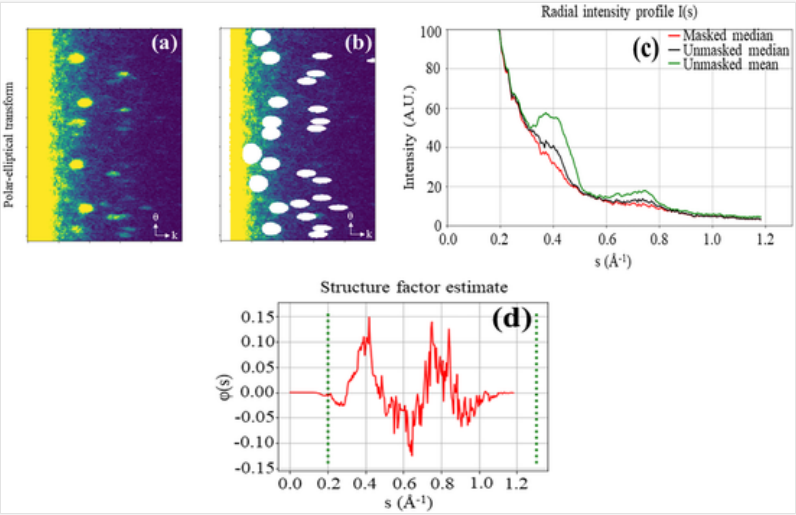

Radial distribution function of the SiOC sample. (a) A calculated radial integral via the polar-elliptical method, without a mask, (b) a calculated radial integral via the polar-elliptical method, with a mask, and (c) radial intensity profiles calculated from (a) and (b), (d) estimated structure factor.

Images are optimised for fast web viewing. Click on the image to view the original version.

alt-text: Fig. 4

~~Fig. 4~~Fig. 4

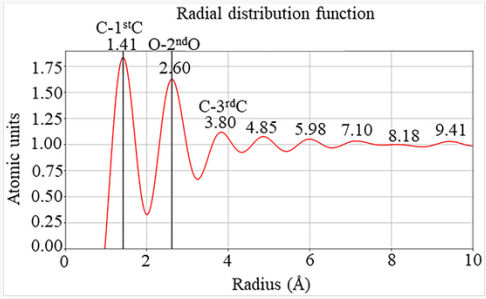

Radial distribution function of the resultant SiOC sample.

The RDF profile based on all images shows the overall features ranging from 1.41 to 9.42 Å. It is well-known that the network of the SiOC ceramic is made up of Si—C and Si—O bonds based on tetrahedral SiO_xC_{4-x} units (X = 0~~-~~4) [6], with the latter atomic pair being dominant [37]. The amount of carbon, which forms during the polymer-to-ceramic transformation process [38], is enough to allow detection of the C—C bonds from the turbostratic carbon or the amorphous SiOC structure consisting of C—C bonds, by the smallest feature located at 1.41 Å in Fig. 4. As for the main characteristic bond distance at 2.60 Å, it is straightforward to assign this feature to the O-2ndO [37] distance from the SiO_2 phase. The peak at 3.80 Å is attributed to the third and its neighbor C-3rdC pair distance [37,39]. At a radial distance over 5 Å, the RDF curve gradually becomes smoother, which means no apparent long-range order exists in the SiOC sample. The findings confirm the structural information of the SiO_xC_{4-x} units in the SiOC through the 4D-STEM-RDF method.

~~3.3.~~3.3 Crystallinity mapping in SiOC

Crystallinity mapping can be determined for the SiOC matrix, which should provide more information about the local structural information. Nanocrystalline SiC embedded in the SiOC amorphous matrix results in local crystallinity variations [40]. Compared to other characterization techniques (NMR imaging, XRD, and neutron diffraction), the 4D-STEM technique [23] provides a map of crystalline phase distribution within an area. SiOC is highly suited for the nanoscale crystallinity mapping due to the low sensitivity to high electron dose bombardment. The small convergence angle and adjustable step size between adjacent measurements make 4D-STEM a powerful tool for studying radiation-sensitive materials. In 4D-STEM, the structures, symmetries, and spacings of Bragg disks in the resulting four-dimensional data hypercube can be used to extract spatially resolved maps of crystalline phases [31]. Redundant information in overlapping Bragg disks can be leveraged to deconvolute the electron beam shape from the SiOC structure.

Bragg disk positions and intensities were used for crystallinity analysis and the local rotation of the crystallites is not determined due to the small sample region. The degree of crystallinity in Fig. 5 carries local structural information, which can be used to characterize the structure of individual phases. Three manually selected areas are shown in Fig. 5, and the Bragg disk features from each pixel position indicate the specific phases. The TEM sample prepared from the powder solution method is relatively thick and results in multi-layered phases. It can be seen that sp^2-bonded carbon sites (turbostratic carbon formed in the carbon-rich SiOC matrix, represented by neighboring cyan dots at the bottom of the middle insert) are around 10 nm upon pyrolysis at 1400 °C, and they are more likely to form in the carbon-rich SiC_xO_{4-x} units (yellow) than in the oxygen-rich SiC_xO_{4-x} units (green), and carbon can form between SiO_2 and SiC with high possibilities. For the turbostratic carbon in the upper left corner of the middle insert, the size is around 3–4 nm. An earlier study [41] reported that the length of turbostratic carbon was ~5 nm in SiOC ceramic pyrolyzed at 1400 °C. Considering that the carbon cluster size is dependent on the polymeric precursor (carbon content) and pyrolysis conditions, these values are consistent. The absence of porosity in the bulk reveals that the free carbon phase is stable, which is consistent with the extraordinary viscoelastic properties of SiOC materials [42]. It also supports the conjecture that the carbon phase behaves as a diffusion barrier and limits the growth of the SiC and SiO_2 clusters. The formation of carbon encapsulating the SiO_2 domains and connecting the SiC domains results in a unique system with good thermal stability. The turbostratic carbon generates an extended region with SiC and SiO_2 domains bonding along its edges. This work highlights the importance of inspection of the Bragg disk positions and intensities in the studies of the degree of crystallinity in SiOCs.

alt-text: Fig. 5

~~Fig. 5~~Fig. 5

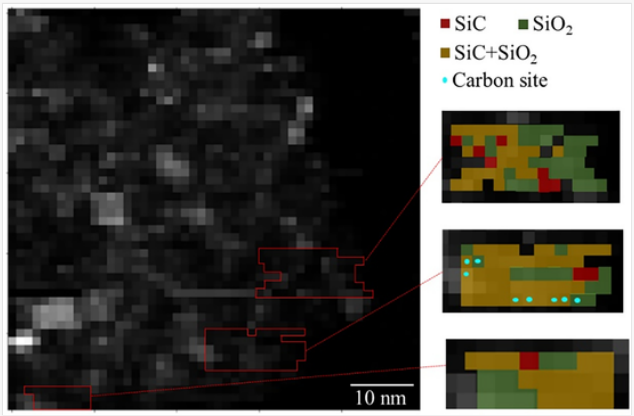

Crystallinity mapping of the SiOC material pyrolyzed at 1400 °C with the presence of specific phases (red-SiC, green-SiO_2, cyan-graphite, and yellow-SiC plus SiO_2). (For interpretation of the references to colour in this figure legend, the reader is referred to the web version of this article.)

Polymer-derived SiOC ceramics are made up of crystalline and amorphous phases, and the corresponding structural inhomogeneity can be assessed by individual diffraction patterns in the 4D-STEM mode with high-speed cameras and high-efficiency pixelated detectors. 4D-STEM-RDF enables a precise interpretation of structural characteristics of amorphous plus crystalline SiOC ceramics. The spatial resolution of the 4D-STEM mode, in this work at ~2 nm, is strongly dependent on the semi-convergence angle, which can be tuned for each application. Finally, uniform and thin sample thickness is helpful for obtaining clean and accurate diffraction patterns in order to avoid the stacking of multiple phases through the sample thickness.

~~4.~~4 Conclusions

This study focuses on an advanced 4D-STEM method for the mixed amorphous and crystalline phase analysis in SiOC. 4D-STEM data preprocessing, including calibration, polar-elliptical coordinate transformation, crystalline diffraction pattern classification, and structure factor/radial distribution function measurements, was carried out using the Python-based py4DSTEM package. The local structure information of the amorphous component of SiOC is presented in the RDF plot to illustrate the bonding topology of the SiOC network. This paper provides the key approaches for single nanometer phase region quantification and should find widespread deployment for highly complex amorphous and crystalline mixed-phase analysis.

Availability of data and material

The raw data required to reproduce these findings are available to download from https://data.lib.vt.edu. The processed data required to reproduce these findings are available to download from https://data.lib.vt.edu.

CRediT authorship contribution statement

Ni Yang: Data curation, Formal analysis, Investigation, Methodology, Validation, Visualization, Writing – original draft, Writing – review & editing. **Colin Ophus:** Conceptualization, Formal analysis, Methodology, Software, Validation, Visualization, Writing – review & editing. **Benjamin H. Savitzky:** Software, Visualization. **Mary C. Scott:** Data curation, Investigation, Writing – review & editing. **Karen Bustillo:** Data curation, Investigation, Writing – review & editing. **Kathy Lu:** Conceptualization, Formal analysis, Funding acquisition, Investigation, Methodology, Project administration, Resources, Supervision, Validation, Writing – original draft, Writing – review & editing.

Declaration of Competing Interest

None.

Acknowledgment

This work was supported by the National Science Foundation under grant numbers CMMI-1634325 and CBET-2024546. Work at the Molecular Foundry was supported by the Office of Science, Office of Basic Energy Sciences, of the U.S. Department of Energy under Contract No. DE-AC02-05CH11231.

~~Appendix A.~~Appendix A Supplementary data

Supplementary data to this article can be found online at https://doi.org/10.1016/j.matchar.2021.111512.

References~~:~~

The corrections made in this section will be reviewed and approved by a journal production editor. The newly added/removed references and its citations will be reordered and rearranged by the production team.

[1] Mu X., Wang D., Feng T., Kübel C., Radial distribution function imaging by STEM diffraction: a method development in resolving the mysteries of amorphous materials, European Microscopy Congress 2016: Proceedings, Wiley Online Library, 2016, pp. 617–618.

[2] Widgeon S.J., Sen S., Mera G., Ionescu E., Riedel R., Navrotsky A., ^{29}Si and ^{13}C solid-state NMR spectroscopic study of nanometer-scale structure and mass fractal characteristics of amorphous polymer derived silicon oxycarbide ceramics, ~~Chemistry of Materials~~Chem. Mater. 22 (2010) 6221–6228.

[3] Lu K., Li J., Fundamental understanding of water vapor effect on SiOC evolution during pyrolysis, ~~Journal of the European Ceramic Society~~J. Eur. Ceram. Soc. 36 (2016) 411–422.

[4] Erb D., Lu K., Additive and pyrolysis atmosphere effects on polysiloxane-derived porous SiOC ceramics, ~~Journal of the European Ceramic Society~~J. Eur. Ceram. Soc. 37 (2017) 4547–4557.

[5] Erb D., Lu K., Effects of SiO_2-forming additive on polysiloxane derived SiOC ceramics, ~~Microporous and Mesoporous Materials~~Microporous Mesoporous Mater. 266 (2018) 75–82.

[6] Yang N., Gao M., Li J., Lu K., Nickel-containing magnetoceramics from water vapor-assisted pyrolysis of polysiloxane and nickel 2, 4-pentanedionate, ~~Journal of the American Ceramic Society~~J. Am. Ceram. Soc. 103 (2020) 145–157.

[7] Lu K., Erb D., Liu M.Y., Thermal stability and electrical conductivity of carbon-enriched silicon oxycarbide, ~~Journal of Materials Chemistry C~~J. Mater. Chem. C 4 (2016) 1829–1837.

[8] Lu K., Li J.K., Fundamental understanding of water vapor effect on SiOC evolution during pyrolysis, ~~Journal of the European Ceramic Society~~J. Eur. Ceram. Soc. 36 (2016) 411–422.

[9] Erb D., Lu K., Influence of vinyl bonds from PDMS on the pore structure of polymer derived ceramics, ~~Materials Chemistry and Physics~~Mater. Chem. Phys. 209 (2018) 217–226.

[10] Yang N., Lu K., Porous and ultrahigh surface area SiOC ceramics based on perhydropolysilazane and polysiloxane, ~~Microporous and Mesoporous Materials~~Microporous Mesoporous Mater. 306 (2020) 110477 (9 pages).

[11] Rau A.V., Knott K., Lu K., Porous SiOC/SiC ceramics via an active-filler-catalyzed polymer-derived method, Mater. Chem. Front. 5 (2021) 6530–6545.

[12] Colombo P., Mera G., Riedel R., Sorarù G.D., Polymer-derived ceramics: 40 years of research and innovation in advanced ceramics, ~~Journal of the American Ceramic Society~~J. Am. Ceram. Soc. 93 (2010) 1805–1837.

[13] Yang N., Lu K., Thermophysical property and electrical conductivity of titanium isopropoxide polysiloxane derived ceramics, ~~Journal of The European Ceramic Society~~J. Eur. Ceram. Soc. 39 (2019) 4029–4037.

[14] Lu K., Erb D., Bawane K., Yang N., Comparison of traditional and flash pyrolysis of different carbon content silicon oxycarbides, ~~Journal of the European Ceramic Society~~J. Eur. Ceram. Soc. 39 (2019) 3035–3041.

[15] Saha A., Raj R., Williamson D.L., A model for the nanodomains in polymer-derived SiCO, ~~Journal of the American Ceramic Society~~J. Am. Ceram. Soc. 89 (2006) 2188–2195.

[16] Dixmier J., Bellissent R., Bahloul D., Goursat P., Neutron diffraction study of the amorphous phase structure in silicon carbonitride ceramics obtained by pyrolysis of a polyvinylsilazane, ~~Journal of the European Ceramic Society~~J. Eur. Ceram. Soc. 13 (1994) 293–298.

[17] Stabler C., Roth F., Narisawa M., Schliephake D., Heilmaier M., Lauterbach S., Kleebe H.-J., Riedel R., Ionescu E., High-temperature creep behavior of a SiOC glass ceramic free of segregated carbon, ~~Journal of the European Ceramic Society~~J. Eur. Ceram. Soc. 36 (2016) 3747–3753.

[18] Xu T., Ma Q., Chen Z., Mechanical property and microstructure evolutions of C_f/SiOC composites with increasing annealing temperature in reduced pressure environment, ~~Ceramics International~~Ceram. Int. 38 (2012) 605–611.

[19] Dubey R.J.C., Sasikumar P.V.W., Cerboni N., Aebli M., Krumeich F., Blugan G., Kravchyk K.V., Graule T., Kovalenko M.V., Silicon oxycarbide-antimony nanocomposites for high-performance Li-ion battery anodes, Nanoscale 12 (2020) 13540–13547.

[20] Mera G., Navrotsky A., Sen S., Kleebe H.-J., Riedel R., Polymer-derived SiCN and SiOC ceramics – structure and energetics at the nanoscale, ~~Journal of Materials Chemistry A~~J. Mater. Chem. A 1 (2013) 3826–3836.

[21] Mu X., Mazilkin A., Sprau C., Colsmann A., Kübel C., Mapping structure and morphology of amorphous organic thin films by 4D-STEM pair distribution function analysis, Microscopy 68 (2019) 301–309.

[22] Ophus C., Ercius P., Sarahan M., Czarnik C., Ciston J., Recording and using 4D-STEM datasets in materials science, ~~Microscopy and Microanalysis~~Microsc. Microanal. 20 (2014) 62–63.

[23] Ophus C., ~~Four-dimensional scanning transmission electron microscopy (4D-STEM): From scanning nanodiffraction to ptychography and beyond~~Four-dimensional scanning transmission electron microscopy (4D-STEM): from scanning nanodiffraction to ptychography and beyond, ~~Microscopy and Microanalysis~~Microsc. Microanal. 25 (2019) 563–582.

[24] Shukla A.K., Ophus C., Gammer C., Ramasse Q., Study of structure of Li-and Mn-rich transition metal oxides using 4D-STEM, ~~Microscopy and Microanalysis~~Microsc. Microanal. 22 (2016) 494–495.

[25] Fang S., Wen Y., Allen C.S., Ophus C., Han G.G., Kirkland A.I., Kaxiras E., Warner J.H., Atomic electrostatic maps of 1D channels in 2D semiconductors using 4D scanning transmission electron microscopy, ~~Nature communications~~Nat. Commun. 10 (2019) 1–9.

[26] Mu X., Neelamraju S., Sigle W., Koch C.T., Toto N., Schön J.C., Bach A., Fischer D., Jansen M., van Aken P.A., Evolution of order in amorphous-to-crystalline phase transformation of MgF_2, ~~Journal of Applied Crystallography~~J. Appl. Crystallogr. 46 (2013) 1105–1116.

[27] Mu X., Mazilkin A., Sprau C., Colsmann A., Kübel C., 4D-STEM pair distribution function mapping of the morphology and structure of amorphous organic materials, ~~Microscopy and Microanalysis~~Microsc. Microanal. 25 (2019) 1944–1945.

[28] Mu X., Wang D., Feng T., Kübel C., ~~Radial distribution function imaging by STEM diffraction: Phase mapping and analysis of heterogeneous nanostructured glasses~~Radial distribution function imaging by STEM diffraction: phase mapping and analysis of heterogeneous nanostructured glasses, Ultramicroscopy 168 (2016) 1–6.

[29] Caplins B.W., Holm J.D., White R.M., Keller R.R., Orientation mapping of graphene using 4D STEM-in-SEM, Ultramicroscopy 113137 (2020).

[30] Zeltmann S.E., Müller A., Bustillo K.C., Savitzky B., Hughes L., Minor A.M., Ophus C., Patterned probes for high precision 4D-STEM bragg measurements, Ultramicroscopy 209 (2020) 112890.

[31] Savitzky B.H., Hughes L.A., Zeltmann S.E., Brown H.G., Zhao S., Pelz P.M., Barnard E.S., Donohue J., DaCosta L.R., Pekin T.C., py4DSTEM: a software package for multimodal analysis of four-dimensional scanning transmission electron microscopy datasets, arXiv preprint (2020) Q7 arXiv:2003.09523.

[32] McAuliffe T., Ackerman A., Savitzky B., Kwok T., Danaie M., Ophus C., Dye D., 4D-STEM elastic Q8 stress state characterisation of a TWIP steel nanotwin, arXiv preprint (2020) arXiv:2004.03982.

[33] Wan W., Sun J., Su J., Hovmöller S., Zou X., Three-dimensional rotation electron diffraction: software RED for automated data collection and data processing, ~~Journal of applied crystallography~~J. Appl. Crystallogr. 46 (2013) 1863–1873.

[34] Craven A., Buggy T., Design considerations and performance of an analytical STEM, Ultramicroscopy 7 (1981) 27–37.

[35] Yang N., Lu K., Porous and ultrahigh surface area SiOC ceramics based on perhydropolysilazane and polysiloxane, ~~Microporous and Mesoporous Materials~~Microporous Mesoporous Mater. 306 (2020) 110477.

[36] Yang N., Lu K., Effects of transition metals on the evolution of polymer-derived SiOC ceramics, Carbon 171 (2021) 88–95.

[37] Brequel H., Soraru G., Schiffini L., Enzo S., ~~Radial distribution function of amorphous silicon oxycarbide compounds~~Radial Distribution Function of Amorphous Silicon Oxycarbide Compounds, J. Metastable Nanocryst. Mater. Trans Tech Publ (2000) 677–682.

[38] Wen Q., Yu Z., Riedel R., The fate and role of in situ formed carbon in polymer-derived ceramics, ~~Progress in Materials Science~~Prog. Mater. Sci. 109 (2020) 100623.

[39] Su Q., Inoue S., Ishimaru M., Gigax J., Wang T., Ding H., Demkowicz M.J., Shao L., Nastasi M., Helium irradiation and implantation effects on the structure of amorphous silicon oxycarbide, ~~Scientific Reports~~Sci. Rep. 7 (2017) 3900.

[40] Panova O., Chen X.C., Bustillo K.C., Ophus C., Bhatt M.P., Balsara N., Minor A.M., Orientation mapping of semicrystalline polymers using scanning electron nanobeam diffraction, Micron 88 (2016) 30–36.

[41] Martínez-Crespiera S., Ionescu E., Kleebe H.-J., Riedel R., Pressureless synthesis of fully dense and crack-free SiOC bulk ceramics via photo-crosslinking and pyrolysis of a polysiloxane, ~~Journal of the European Ceramic Society~~J. Eur. Ceram. Soc. 31 (2011) 913–919.

[42] Kleebe H.-J., Blum Y.D., SiOC ceramic with high excess free carbon, ~~Journal of the European Ceramic Society~~J. Eur. Ceram. Soc. 28 (2008) 1037–1042.

Graphical abstract

Images are optimised for fast web viewing. Click on the image to view the original version.

alt-text: Unlabelled Image

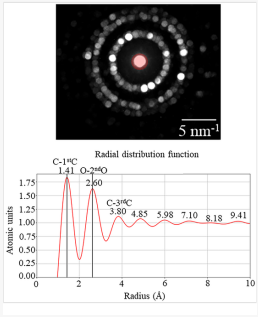

Highlights

- A 4D-STEM method for analysis of mixed amorphous and crystalline phases was given.
- 4D-STEM data preprocessing was carried out using py4DSTEM package.
- Local structure of amorphous SiOC illustrates bonding topology of SiOC network.
- Key approaches for single nanometer phase region quantification are provided.

~~Appendix A.~~ Appendix A Supplementary data

Multimedia Component 1

Supplementary material

alt-text: Image 1

Queries and Answers

Q1

Query: Your article is registered as a regular item and is being processed for inclusion in a regular issue of the journal. If this is NOT correct and your article belongs to a Special Issue/Collection please contact r.nahid@elsevier.com immediately prior to returning your corrections.

Answer: Yes

Q2

Query: Please confirm that given names and surnames have been identified correctly and are presented in the desired order, and please carefully verify the spelling of all authors' names.

Answer: Yes

Q3

Query: The author names have been tagged as given names and surnames (surnames are highlighted in teal color). Please confirm if they have been identified correctly.

Answer: Yes

Q4

Query: Have we correctly interpreted the following funding source(s) and country names you cited in your article: "National Science Foundation; Office of Science; Basic Energy Sciences; U.S. Department of Energy".

Answer: Yes

Q5

Query: Supplementary caption was not provided. Please check the suggested data if appropriate, and correct if necessary.

Answer: The supplement file is ok.

Q6

Query: Supplementary caption was not provided. Please check the suggested data if appropriate, and correct if necessary.

Answer: The supplement file is ok.

Q7

Query: Please provide the volume number and page range for the bibliography in Ref. [31].

Answer: This is the way it is available. The pages are 1-32.

Q8

Query: Please provide the volume number and page range for the bibliography in Ref. [32].

Answer: This is the way it is available. The pages are 1-5.